Measurement of the electronic transition dipole moment by Autler-Townes splitting: Comparison of three- and four-level excitation schemes for the Na_2 $A\,^1\Sigma_u^+ - X\,^1\Sigma_g^+$ system

E. Ahmed, A. Hansson,[a] P. Qi, T. Kirova, A. Lazoudis, S. Kotochigova, and A. M. Lyyra[b]
Department of Physics, Temple University, Philadelphia, Pennsylvania 19122-6082

L. Li
Department of Physics and Key Laboratory of Atomic and Molecular Nanosciences, Tsinghua University, Beijing 100084, China

J. Qi
Department of Physics/Astronomy Penn State Berks, Tulpehocken Road, P.O. Box 7009, Reading, Pennsylvania 19610

S. Magnier
IUFM de Bretagne, 153 rue Saint Malo, CS 54310, F-35042 Rennes Cedex, France and Laboratoire de Physique des Atomes, Lasers, Molecules et Surfaces (PALMS), CNRS et Université Rennes 1 (UMR 6627), Campus de Beaulieu, Bâtiment 11B, F-35043 Rennes Cedex, France

(Received 9 September 2005; accepted 13 December 2005; published online 24 February 2006)

We present a fundamentally new approach for measuring the transition dipole moment of molecular transitions, which combines the benefits of quantum interference effects, such as the Autler-Townes splitting, with the familiar *R*-centroid approximation. This method is superior to other experimental methods for determining the absolute value of the *R*-dependent electronic transition dipole moment function $\mu_e(R)$, since it requires only an accurate measurement of the coupling laser electric field amplitude and the determination of the Rabi frequency from an Autler-Townes split fluorescence spectral line. We illustrate this method by measuring the transition dipole moment matrix element for the Na_2 $A\,^1\Sigma_u^+$ $(v'=25,\ J'=20e)$-$X\,^1\Sigma_g^+$ $(v''=38,\ J''=21e)$ rovibronic transition and compare our experimental results with our *ab initio* calculations. We have compared the three-level (cascade) and four-level (extended Λ) excitation schemes and found that the latter is preferable in this case for two reasons. First, this excitation scheme takes advantage of the fact that the coupling field lower level is outside the thermal population range. As a result vibrational levels with larger wave function amplitudes at the outer turning point of vibration lead to larger transition dipole moment matrix elements and Rabi frequencies than those accessible from the equilibrium internuclear distance of the thermal population distribution. Second, the coupling laser can be "tuned" to different rovibronic transitions in order to determine the internuclear distance dependence of the electronic transition dipole moment function in the region of the *R*-centroid of each coupling laser transition. Thus the internuclear distance dependence of the transition moment function $\mu_e(R)$ can be determined at several very different values of the *R* centroid. The measured transition dipole moment matrix element for the Na_2 $A\,^1\Sigma_u^+$ $(v'=25,\ J'=20e)$-$X\,^1\Sigma_g^+$ $(v''=38,\ J''=21e)$ transition is 5.5 ± 0.2 D compared to our *ab initio* value of 5.9 D. By using the *R*-centroid approximation for this transition the corresponding experimental electronic transition dipole moment is 9.72 D at $R_c=4.81$ Å, in good agreement with our *ab initio* value of 10.55 D. © *2006 American Institute of Physics*.
[DOI: 10.1063/1.2164454]

I. INTRODUCTION

Coherence effects such as electromagnetically induced transparency[1] (EIT) and Autler-Townes (AT) splitting[2] have attracted a great deal of attention recently. Many investigations, complementary to EIT, also include an exploration of the AT effect, which considerably modifies the observed spectra that characterize the laser interaction with the medium. In most experiments the modification caused by the stronger coupling field is observed in the spectrum resulting from the scan of the weaker probe laser.

These quantum interference effects have been observed in atoms using complicated multilevel systems with different energy level arrangements.[3–9] Yan *et al.*[9] have experimentally demonstrated suppression of two-photon absorption due to EIT in a four-level inverted-Y system of cold ^{87}Rb atoms. In their theoretical analysis of a similar closed system Joshi and Xiao[10] demonstrated the ability to control the EIT characteristics in the system by manipulating various parameters such as lifetimes and laser detuning values.

It has been more difficult to extend these studies to mo-

[a]Permanent address: Department of Physics, Stockholm University, Alba Nova, SE–10691 Stockholm, Sweden.
[b]Author to whom correspondence should be addressed. Electronic mail: Lyyra@temple.edu

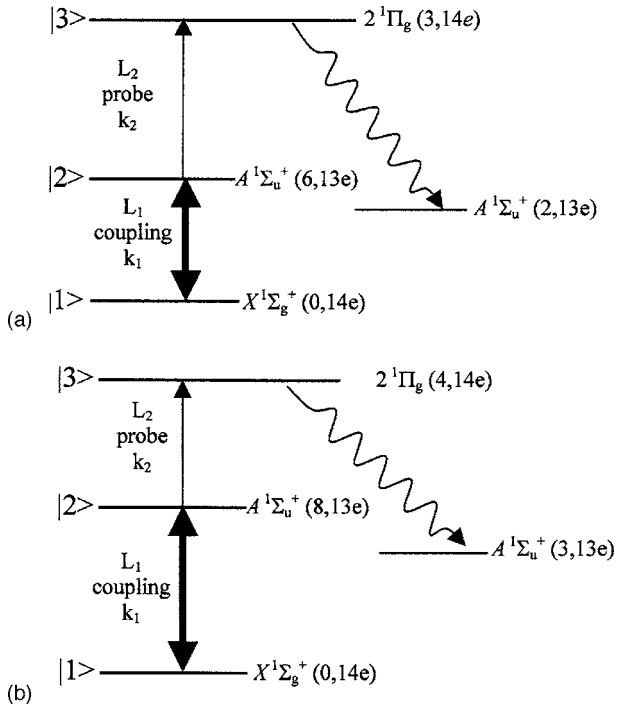

FIG. 1. Energy-level diagrams for the three-level (two laser) cascade excitation schemes. The lasers L_1 and L_2 are in a counterpropagating arrangement. (a) $|1\rangle$ is the ground state $X\,^1\Sigma_g^+$ $(v''=0,\ J''=14e)$, $|2\rangle$ is the intermediate state $A\,^1\Sigma_u^+$ $(v'=6,\ J'=13e)$, and $|3\rangle$ is the upper state $2\,^1\Pi_g$ $(v=3,\ J=14e)$. The laser wave numbers corresponding to the resonance transitions $|2\rangle \leftarrow |1\rangle$ and $|3\rangle \leftarrow |2\rangle$ for the molecules with zero velocity in the laser propagation direction $(v_L=0)$ are $k_1=15\,335.827\ \mathrm{cm}^{-1}$ and $k_2=15\,511.066\ \mathrm{cm}^{-1}$, respectively. The k_1/k_2 ratio is 0.989 in this case. (b) $|1\rangle$ is the ground state $X\,^1\Sigma_g^+$ $(v''=0,\ J''=14e)$, $|2\rangle$ is the intermediate state $A\,^1\Sigma_u^+$ $(v'=8,\ J'=13e)$, and $|3\rangle$ is the upper state $2\,^1\Pi_g$ $(v=4,\ J=14e)$. The laser wave numbers corresponding to the resonance transitions $|2\rangle \leftarrow |1\rangle$ and $|3\rangle \leftarrow |2\rangle$ for the molecules with zero velocity in the laser propagation direction $(v_L=0)$ are $k_1=15\,559.153\ \mathrm{cm}^{-1}$ and $k_2=15\,387.259\ \mathrm{cm}^{-1}$, respectively. The k_1/k_2 ratio is 1.011 in this case.

lecular systems.[11–18] This is due to the fact that the critical parameter in these studies, the Rabi frequency $\Omega=\mu E/\hbar$, is much smaller for any molecular rovibronic transition than that in an atomic system because the transition dipole moment matrix elements μ for molecular transitions are small compared to atomic ones, and the E-field amplitudes associated with commercially available narrow band continuous wave lasers are modest and thus the available Rabi frequencies for molecular transitions are limited in high-resolution experiments. In order to avoid masking of the coherence effects by the laser power saturation broadening effects, the power of all lasers with the exception of the coupling laser was kept as low as possible without compromising the signal-to-noise ratio. Furthermore, by avoiding coupling laser transitions that involve the lowest ground state vibrational levels in the thermal population range with smaller Franck-Condon factors with excited states, multiple-resonance excitation schemes can be used to exploit larger rovibronic wave function amplitudes at the intermediate to large internuclear distance leading to large Franck-Condon factors and Rabi frequencies (see Figs. 1 and 2).[15] In addition, by using a judicious choice of laser propagation geometry and the ratio of the probe and coupling laser wave numbers,[19] it has been shown that despite the presence of Doppler broadening, it has been possible to observe these effects in molecular samples with moderate Rabi frequencies for rovibronic transitions.[15,16,20,21] The Autler-Townes effect has also been observed in a molecular beam environment[22] and in ultracold molecules.[23–25]

In our earlier works[15,16,26] we have demonstrated that the AT effect can be used to control molecular angular momentum alignment and to expand molecular rovibronic state selectivity all-optically to magnetic sublevels by using the all-optical triple resonance excitation technique.[27] It has been shown that for molecules in the gas phase, it is possible to obtain the absolute value of the transition dipole moment matrix element[11,16,22] between *excited* electronic states by measuring the AT splitting in these states.

In this paper we investigate the possibility of determining the transition dipole moment matrix element for the molecular transition between the ground state and the first excited state by exploring two excitation schemes with different energy level configurations: a three-level cascade scheme using double resonance excitation (Fig. 1) and a four-level extended Λ scheme using triple resonance excitation (Fig. 2). Since the coupling field in the three-level cascade case involves a laser excitation between the ground state and the first excited state, the three-level system, although experimentally simpler, is expected to be less favorable. This is because the coupling laser transition from the ground state to the first excited state is Doppler broadened and the higher coupling laser power is expected to result in lower resolution because of saturation broadening. In addition, the available coupling laser Rabi frequencies are limited by the Franck-Condon factors available for excitation from levels in the thermally populated range of the ground state in this particular case.

We expect the four-level system to be more advantageous in that a coupling laser transition outside the constraints of internuclear distance of the thermal population is now possible with a much larger transition dipole moment matrix element, leading to a larger coupling laser Rabi frequency (Fig. 3). This in turn results in a larger AT splitting and a better resolved AT splitting spectrum. In addition, in the four-level case, a low power narrow band pump laser is used to select a narrow velocity group from the Doppler-broadened transition as in Ref. 15 to enhance the resolution of the probe laser scan, the sole purpose of which is to reveal the Autler-Townes splitting of the intermediate level. In this case the topmost rovibronic state $|3\rangle$ is unaffected by the coupling field and is not expected to affect the appearance of the probe laser scan.

Other traditional experimental methods to measure the variation of the transition dipole moment as a function of internuclear distance involve the measurement of either molecular fluorescence or absorption intensities,[28–30] or the measurement of radiative lifetimes.[31,32] It is well known that absolute intensity measurements are very difficult because of the need to calibrate with high accuracy the wavelength and polarization dependence of the detection system. In addition, it is difficult to determine molecular densities very accurately. As a result, the transition dipole moments resulting from such experiments are relative. Lifetime measurements,

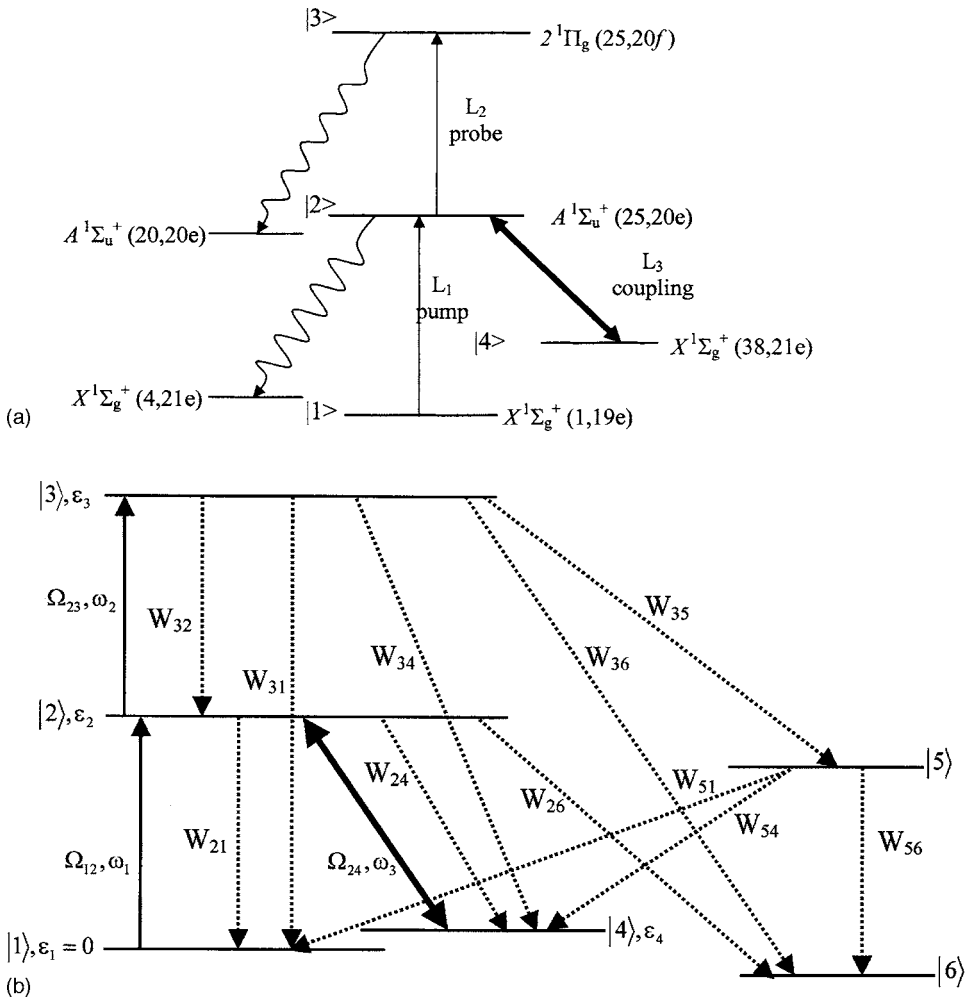

FIG. 2. (a) Energy-level diagram for the four-level system with triple resonance excitation. The pump and probe lasers, L_1 and L_2, are in a copropagating arrangement and counterpropagate with the coupling field L_3. $|1\rangle$ denotes the initial level of L_1 $X\,^1\Sigma_g^+$ ($v''=1$, $J''=19e$), $|2\rangle$ denotes the intermediate state $A\,^1\Sigma_u^+$ ($v'=25$, $J'=20e$), which is the terminal level of L_1 and initial level of L_2, $|3\rangle$ denotes the upper state level to which the probe L_2 is tuned $2\,^1\Pi_g$ ($v=25$, $J=20f$), and $|4\rangle$ is the lower level $X\,^1\Sigma_g^+$ ($v''=38$, $J''=21e$) of the coupling field resonance transition. The wave numbers associated with the transition resonance frequencies are $k_1=17\,187.612$ cm^{-1}, $k_2=15\,519.871$ cm^{-1}, and $k_3=12\,546.693$ cm^{-1}. (b) A schematic diagram of excitation and decay processes of the Na_2 four-level triple resonance experiment. Due to selection rules W_{31}, W_{34}, and W_{36} are zero in this particular case. The energy levels $|1\rangle$, $|2\rangle$, $|3\rangle$, and $|4\rangle$ signify the rovibronic energy levels of (a). The solid arrows indicate the lasers with Rabi and photon frequencies specified. The dashed arrows indicate possible decay channels from the different energy levels. Levels $|5\rangle$ and $|6\rangle$ indicate other possible decay channels rendering the system open. W_{ji} denotes the total decay rate between levels $|j\rangle$ and $|i\rangle$ which affect the populations of the levels involved as well as the decay rates of the coherences.

on the other hand, suffer from the additional problem that each lifetime is related to a complicated average of the transition moment squared over a wide range of lower states. In addition, systematic errors can be sometimes difficult to identify.[33]

In addition to these more conventional methods, optically pumped laser (OPL) gain measurements have also been investigated in this context.[34] These measurements also led to relative transition dipole moment values due to complications caused by gain competition effects, power and pressure broadenings, intracavity absorption losses, and wavelength-dependent diffraction losses.

In contrast to these difficulties the critical measurements in the Autler-Townes splitting based method are the accurate measurements of the electric field amplitude E of the coupling laser and the Autler-Townes split fluorescence line profile. This spectral line profile can then be used to determine the Rabi frequency $\Omega=\mu E/\hbar$, which directly yields the transition dipole moment matrix element μ. Earlier experiments[11,16,22] based on the Autler-Townes splitting were limited to the internuclear distance range accessible from the thermal population in the ground electronic state only. By using the triple resonance excitation approach, different combinations of vibrational levels for the coupling field transition (v',v'') in the excited state and the ground state can be used to probe the R dependence of the transition dipole moment function by using the R-centroid approximation.[35–44] Thus we expect that the experimentally measured transition dipole moment matrix element values can be used to determine the absolute value of the R-dependent electronic transition dipole moment function over a wide range of R. This is based on the idea that the coupling laser probes the electronic transition dipole moment in the region of the R-centroid value determined by the rovibronic wave functions associated with the coupling field transition. According to the R-centroid approximation,

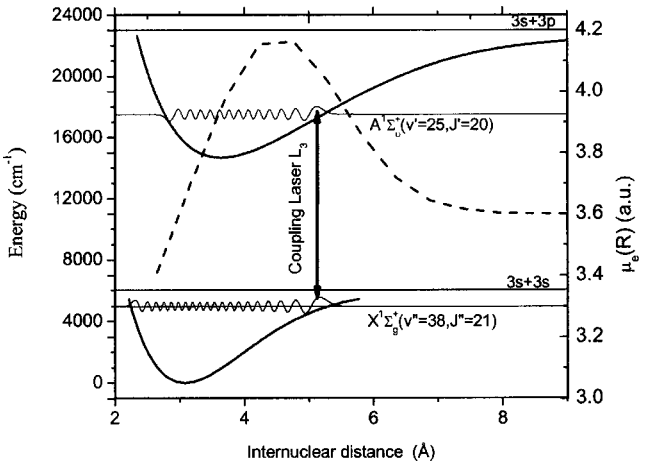

FIG. 3. The dashed line represents the calculated electronic transition dipole moment using the pseudopotential method for the Na_2 $A\,^1\Sigma_u^+$-$X\,^1\Sigma_g^+$ resonance transition as function of the internuclear distance R. The potential curves of the $X\,^1\Sigma_g^+$ and $A\,^1\Sigma_u^+$ states as well as the rovibronic wave functions are also given for the $X\,^1\Sigma_g^+$ $(v''=38,\ J''=21e) \rightarrow A\,^1\Sigma_u^+$ $(v'=25,\ J'=20e)$ transitions.

$$|\langle v'J'|\mu_e(R)|v''J''\rangle| \sim |\mu_e(R_c)||\langle v'J'|v''J''\rangle|, \qquad (1)$$

$$R_c = \frac{\langle v'J'|R|v''J''\rangle}{\langle v'J'|v''J''\rangle},$$

where $\mu_e(R)$ is the R-dependent electronic transition dipole moment function, R_c is the R-centroid, and $\langle v'J'|v''J''\rangle$ is the vibrational overlap factor corresponding to the rovibronic states v', J' and v'', J'' associated with the coupling laser. Classically electronic transitions terminate at the points of internuclear distance that conserve nuclear position and momentum. Quantum mechanically this is in conflict with the uncertainty principle and thus the overlap integrals have to be evaluated over the entire region including the nonclassical region. As indicated by Tellinghuisen[42] the semiclassical stationary phase approximation reconciles the classical and quantum interpretations since the integrals involving the vibrational wave functions accumulate mostly in the region of the classical transition points, which are the points of stationary phase. When a single point of stationary phase exists, that point corresponds to the R-centroid value. For multiple points of stationary phase this correspondence with the point of stationary phase and the R-centroid value is less clear. However, Noda and Zare[43] have introduced a generalized method of subdividing the range of the numerical integration in order to overcome these difficulties. Since vibrational wave functions have large amplitudes at very large internuclear distance close to the dissociation limit, additional complications may arise. However, in this region the electronic transition dipole moment approaches the separated atom limit value. Thus we expect to be able to combine the Autler-Townes quantum interference effect and the R-centroid approximation to a powerful new and generally applicable method to sample the transition dipole moment function at several very different values of the R-centroid by simply measuring the electric field amplitude of the coupling laser and the Autler-Townes split spectral line profile of the coupling laser transitions corresponding to different R-centroid values.

II. EXPERIMENTAL DETAILS

The experimental arrangement was nearly the same as described previously.[15,16] Sodium vapor was generated in a five-arm heatpipe oven. Argon gas was used as a buffer gas with about 100–200 mTorr pressure. The corresponding vapor temperature was about 600 K. Two Coherent Autoscan 699-29 dye lasers and a Coherent 899-29 Titanium Sapphire laser, all with 0.5 MHz frequency bandwidth, were used in our experiment. The laser beams were linearly polarized in the same direction. In the three-level (double resonance or cascade) excitation scheme [see Figs. 1(a) and 1(b)] the two dye lasers were counterpropagating. In the four-level (triple resonance or extended Λ configuration) excitation scheme [see Fig. 2(a)] the two dye laser beams copropagated in the opposite direction of the coupling field (Coherent 899-29 Titanium Sapphire laser). A mechanical chopper was used to modulate one of the laser beams for phase-sensitive detection. A SPEX 1404 double grating monochromator was used to detect the molecular fluorescence of a selected single rovibronic fluorescence transition in a direction perpendicular to the laser propagation direction. When the probe laser frequency was scanned, the output of the monochromator photomultiplier tube (PMT) was used as input to a lock-in amplifier (SR 850) with its output recorded by the computer that also controlled the laser scan. Neutral density filters were used to control the power of the lasers, and the spot sizes of the laser beams were measured carefully in the interaction region with a razor blade technique.[45] Initially the two or three laser beams were carefully overlapped by maximizing the optical-optical double resonance (OODR) fluorescence signal in the case of the three-level system, while for the four-level extended Λ scheme, various combinations of two laser OODR fluorescence signals were used. After that for a finer adjustment of the overlap, especially in the three-laser experiments, we used the magnitude of the observed AT splitting to maximize the overlap. Once the best possible overlap was achieved it was kept unchanged during the full length of the particular set of experiments. In order to ensure E field homogeneity of the coupling field in the interaction region the spot size of the coupling laser was kept about twice as large as the probe and pump laser spot sizes. The spot size is defined here as a diameter, measured at the $1/e^2$ points of the Gaussian beam profile. It was important to have such an arrangement in order to make the theoretical interpretation of the experimental spectra easier. Tighter focusing of the pump and probe lasers restricted the observed fluorescence to the center of the radial distribution of the Gaussian coupling laser electric field amplitude, and thus the molecules in the overlap region experienced a more uniform coupling laser electric field leading to a better resolved AT splitting line profile. The desirable spot size for each laser was obtained with a lens or a combination of two lenses. In the three-level system the beam diameters during the experiments at the center of the heatpipe were 680 μm for the coupling field (L_1) and 290 μm for the probe laser (L_2)

beam. In the extended Λ (triple resonance) scheme [see Fig. 2(a)] the beam diameters were 560, 460, and 1020 μm for the pump laser beam (L_1), probe laser beam (L_2), and coupling field (L_3) laser beam, respectively. We took special care to make the coupling laser electric field profile homogeneous along the propagation direction of the lasers, and especially across the 2.5-cm-long overlap region from which the detected fluorescence was collected. For optimal collimation of the coupling laser beam two lenses were used with appropriately chosen focal lengths. We have estimated by repeated trials that the error of our spot size measurement is about 10 μm, which is also the smallest step size of the micrometer we used to drive the razor blade across the beam profile for the beam diameter measurement.[45] The power of the laser beams was measured with Coherent Lasermate/D power meter with absolute accuracy of about 1.5%.

III. EXCITATION SCHEMES

The details of the two excitation schemes used in this work to probe the $A\ ^1\Sigma_u^+$-$X\ ^1\Sigma_g^+$ of Na_2 transition dipole moment are shown in Figs. 1 and 2. The cascade double resonance excitation scheme with $|k_1/k_2|<1$ and >1 is shown in Figs. 1(a) and 1(b), respectively. The labeling of the vibrational and rotational quantum numbers involves double prime and prime notation for the ground state and the first excited state, respectively. In addition, the rotational levels are labeled with e symmetry, if a rotational level with (+) parity has $(+)(-1)^J=1$, and with f symmetry, if (+) $\times(-1)^J=-1$. Similarly, if a level with (−) parity has (−) $\times(-1)^J=1$, the level is labeled by e symmetry, and if (−) $\times(-1)^J=-1$ its symmetry label is f.[46,47] In Fig. 1(a) the coupling laser L_1 is tuned to resonance on the $A\ ^1\Sigma_u^+(v'=6,\ J'=13e)$-$X\ ^1\Sigma_g^+(v''=0,\ J''=14e)$ transition. In this case the probe laser L_2 upper level is $2\ ^1\Pi_g(v=3,\ J=14e)$. In Fig. 1(b) the coupling field (L_1) transition is $A\ ^1\Sigma_u^+\ (v'=8,\ J'=13e)$-$X\ ^1\Sigma_g^+\ (v''=0,\ J''=14e)$, the probe laser ($L_2$) upper level transition is $2\ ^1\Pi_g\ (v=4,\ J=14e)$, and $|k_1/k_2|>1$ as a result. In both cases the initial level of L_1 is in the thermal population range. The probe laser (L_2) was used to probe the Autler-Townes splitting of the intermediate level $|2\rangle$ caused by the coupling field.

In the triple resonance excitation scheme, shown in Fig. 2(a) the coupling laser (L_3) transition was chosen so that the lower level of the $A\ ^1\Sigma_u^+\ (v'=25,\ J'=20e)$-$X\ ^1\Sigma_g^+\ (v''=38,\ J''=21e)$ transition was outside the range of the ground state thermal population. A weak pump laser (L_1) was tuned to resonance on the $A\ ^1\Sigma_u^+\ (v'=25,\ J'=20e)$-$X\ ^1\Sigma_g^+\ (v''=1,\ J''=19e)$ transition with the initial level in the thermal population range. The power of this laser was kept as low as possible to define a narrow velocity component within the Doppler profile. The Autler-Townes splitting of level $|2\rangle$ was then detected in the fluorescence spectrum of a rovibronic transition resulting from the scan of the weak probe laser (L_2) through the $2\ ^1\Pi_g\ (v=25,\ J=20f)$-$A\ ^1\Sigma_u^+\ (v'=25,\ J'=20e)$ transition.

Figure 2(b) illustrates the various excitation and decay processes of this open molecular system that were used in the following theoretical analysis needed to interpret our experimental results. The energy levels $|1\rangle$, $|2\rangle$, $|3\rangle$, and $|4\rangle$ signify the rovibronic energy levels of Fig. 2(a). The solid arrows indicate the lasers with Rabi and photon frequencies specified. The dashed arrows indicate the possible decay channels from the different energy levels. Levels $|5\rangle$ and $|6\rangle$ indicate other possible decay channels rendering the system open. W_{ji} denotes the total decay rate between levels $|j\rangle$ and $|i\rangle$ which affect the populations of the levels involved as well as the decay rates of the coherences.

IV. THEORETICAL CALCULATIONS

Since the goal of this project was to determine the transition dipole matrix element from experimentally observed Autler-Townes splitting spectra and to compare that value with theoretical values based on *ab initio* transition dipole moments, the simulations required the use of the density matrix formalism[48–51] (see Sec. IV A). For a comparison of our results with theoretical transition dipole moment values, we also present here *ab initio* transition moments calculated using both the configuration-interaction pseudopotential method and the relativistic configuration-interaction method (see Sec. IV B). In addition, the radiative lifetimes of the excited states play an important role in the simulations. These lifetimes are not affected by nonradiative processes such as predissociation or collisions. When experimental or calculated lifetime values were not available, we calculated the values of lifetimes in order to eliminate possible errors caused by using guesses for the values of these parameters. Our lifetime calculations are described in Sec. IV B 3.

A. Density-matrix formalism

For the simulation of our experimental results we followed standard density matrix formalism. Accordingly the density matrix equation of motion for the nmth matrix element is given by

$$\dot{\rho}_{nm} = -\frac{i}{\hbar}\sum_k (H_{nk}\rho_{km} - \rho_{nk}H_{km}) + \text{relaxation terms}, \quad (2)$$

where $H_{nk}=\langle n|H|k\rangle$. The Hamiltonian H for the three- and four-level systems has the following forms.

Three-level system:

$$H = \hbar\Delta_1|2\rangle\langle 2| + \hbar(\Delta_1+\Delta_2)|3\rangle\langle 3| + \hbar\frac{\Omega_{12}}{2}(|1\rangle\langle 2| + |2\rangle\langle 1|) + \hbar\frac{\Omega_{23}}{2}(|2\rangle\langle 3| + |3\rangle\langle 2|). \quad (3)$$

Four-level system:

$$H = \hbar\Delta_1|2\rangle\langle 2| + \hbar(\Delta_1+\Delta_2)|3\rangle\langle 3| + \hbar(\Delta_1+\Delta_3)|4\rangle\langle 4| + \hbar\frac{\Omega_{12}}{2}(|2\rangle\langle 1| + |1\rangle\langle 2|) + \hbar\frac{\Omega_{23}}{2}(|3\rangle\langle 2| + |2\rangle\langle 3|) + \hbar\frac{\Omega_{24}}{2}(|4\rangle\langle 2| + |2\rangle\langle 4|). \quad (4)$$

In the expression above we define the velocity-dependent detuning of the pump, probe, and coupling lasers from mo-

lecular transitions as $\Delta_1 \equiv \omega_{21} - \omega_1 + k_1 v_z$, $\Delta_2 \equiv \omega_{32} - \omega_2 + k_2 v_z$, and $\Delta_3 \equiv \omega_3 - \omega_{24} + k_3 v_z$, respectively. Here k_1, k_2, and k_3 are the wave numbers of the corresponding laser beams and v_z is the molecular velocity along the laser propagation direction. When the lth laser is tuned near resonance with the $|i\rangle, |i+1\rangle$ transition, the Rabi frequency at the distance r from the beam axis is expressed as

$$\Omega_{l,M}(r) \equiv \left(\frac{\mu_{i,i+1}(M)E_l}{\hbar}\right)\exp\left(-\frac{4r^2}{w_l^2}\right), \tag{5}$$

where $\mu_{i,i+1}(M) = \langle \psi_{v'j'} | \mu_e(R) | \psi_{v''j''} \rangle$ is the magnetic sublevel M-dependent transition dipole moment matrix element, and w_l and E_l are the beam spot size (diameter) and the electric field amplitude, respectively, of the lth laser beam. $\mu_e(R)$ denotes the electronic transition dipole moment as a function of internuclear distance R.

The relaxation terms in Eq. (2) phenomenologically account for the spontaneous decay of the levels and the collisional dephasing:

$$\gamma_{nm} = \frac{1}{2}\sum_k (W_{nk} + W_{mk}) + \gamma_{nm}^{\text{collisional}}, \quad n \neq m. \tag{6}$$

The population decay rate W_n of level n is defined as $W_n = \Sigma_k W_{nk}$ (k runs over all levels lower than n) and the summation includes all possible emission paths [see Fig. 2(b)]. A beam-transit rate is added for level $|4\rangle$ because of its slow decay rate. This is the rate with which the molecules escape the interaction region. We have calculated it according to Sagle *et al.*[52]

Because only cw lasers are involved in our experiments, a steady state approximation is made in the Eq. (2), which transforms them from a set of differential equations of first order to a simple set of homogeneous linear equations. The set of linear equations obtained in such a way for the three- and four-level systems is solved numerically for the population of level $|3\rangle$, along with the condition for conservation of the population in the system. The latter transforms essentially the homogeneous system of linear equations obtained through the steady state approximation to an inhomogeneous one. In our open molecular system, the total population of the three (four) coherently coupled levels $|1\rangle$, $|2\rangle$, $|3\rangle$, and $|4\rangle$ (for the four-level system) compared to a closed atomic case is no longer conserved. Thus two auxiliary states $|5\rangle$ and $|6\rangle$ are incorporated, representing all other vibrational states of the A and X manifolds, respectively, to which decays are possible. Then the population conservation condition can be written as

$$N = \rho_{11} + \rho_{22} + \rho_{33} + \rho_{55} + \rho_{66}, \quad \text{three-level system},$$

$$N = \rho_{11} + \rho_{22} + \rho_{33} + \rho_{44} + \rho_{55} + \rho_{66}, \quad \text{four-level system}.$$

The population of level $|3\rangle$, up to a constant of proportionality, can be interpreted as the experimentally recorded single-channel (specific rovibrational decay path) fluorescence as a function of the detuning of the probe laser.

TABLE I. Tabulated absolute values of the transition dipole moments between the ground $X\,^1\Sigma_g^+$ and the excited $A\,^1\Sigma_u^+$ states of Sodium dimer as a function of the internuclear separation R using pseudopotential *ab initio* calculations.

R (a.u.)	$\mu_e(R)$ (D)	R (a.u.)	$\mu_e(R)$ (D)
5	8.67	18	9.12
6	9.42	19	9.11
7	10.12	20	9.10
8	10.56	22	9.08
9	10.58	24	9.06
10	10.24	26	9.05
11	9.80	28	9.04
12	9.45	30	9.03
13	9.26	32	9.03
14	9.19	34	9.02
15	9.16	36	9.02
16	9.15	38	9.02
17	9.14	40	9.02

B. Transition dipole moment calculations

In order to compare our experimental results with the theoretical results, *ab initio* transition dipole moments have been calculated using the configuration-interaction pseudopotential method as well as the relativistic configuration-interaction method as described in the following.

1. Pseudopotential calculation

The transition dipole moment between electronic states of Na_2 has been computed over a large range of internuclear distance ($5a_0 < R < 40a_0$). Molecular energies and two-electron wave functions have been determined through configuration-interaction (CI) calculations in the framework of pseudopotential method. Details of the method and the basis sets used in this work may be found in Ref. 53. The expectation value of the operator $\sum_{i=1}^{2} \mathbf{r}_i$ has been estimated on the basis set of CI two-electron wave functions. The absolute values of the transition dipole moment for the transition $A\,^1\Sigma_u^+$-$X\,^1\Sigma_g^+$ are listed in Table I as a function of internuclear distance and graphically illustrated in Fig. 3. The transition dipole moment for the $A\,^1\Sigma_u^+ (v'=25, J'=20e)$-$X\,^1\Sigma_g^+ (v''=38, J''=21e)$ transition using the $\mu_e(R)$ calculated from this method is 5.93 D.

2. Relativistic configuration-interaction calculation

Since the Na_2 $A\,^1\Sigma_u^+$ and $b\,^3\Pi_u$ states are mixed by the spin-orbit interaction, we have also used the relativistic configuration-interaction valence bond method[54] to calculate electric dipole transition moments of the Na_2 molecule as a function of internuclear separation. We calculated transition dipole moments between the ground state and the $A\,^1\Sigma_u^+$ and $b\,^3\Pi_u$ excited state potentials, dissociating to the Na(3*s*) +Na(3*p*) limits. The nonzero transition from the $X\,^1\Sigma_g^+$ ground state to the $b\,^3\Pi_u$ state is only allowed due to relativistic spin-orbit coupling. The accuracy of the calculation of the $X\,^1\Sigma_g^+$, $A\,^1\Sigma_u^+$, and $b\,^3\Pi_u$ molecular electronic wave

functions is tested by comparing our *ab initio* potentials with existing experimental potentials.[55–58]

In our approach the molecular electronic wave function $|\Psi_{AB}\rangle$ is constructed from wave functions, which are products of wave functions that describe the constituent atoms A and B. In essence, the molecular wave function is given by

$$|\Psi_{AB}\rangle = \sum C_\alpha |\det_\alpha^{AB}\rangle, \tag{7}$$

where each $|\det_\alpha^{AB}\rangle$ is an antisymmetrized $(\hat{A})$ product of two atomic Slater determinants,

$$|\det_\alpha^{AB}\rangle = \hat{A}(|\det_\alpha^{A}\rangle |\det_\alpha^{B}\rangle). \tag{8}$$

The atomic Slater determinants $|\det_\alpha^{A}\rangle$ and $|\det_\alpha^{B}\rangle$ are constructed from one-electron four-component Dirac spinors centered on the nucleus of atoms A and B, respectively. The CI coefficients C_α in Eq. (7) are obtained by solving a generalized eigenvalue matrix problem, where the $|\det_\alpha^{AB}\rangle$ are not orthogonal.

The molecular transition dipole moment between $|a\rangle$ and $|b\rangle$ molecular states as a function of internuclear distance R is calculated from

$$\mu_{ba}(R) = \langle \Psi_{AB}^b(R) | \sum_{i=1}^{N} e\mathbf{r}_i | \Psi_{AB}^a(R)\rangle, \tag{9}$$

where N is the total number of electrons in the molecule, e is the electron charge, and $\mathbf{r}_i$ is the electron position vector.

Dirac spinors are obtained by self-consistently solving Dirac-Fock and Sturmian equations.[54] We use single-electron Dirac-Fock functions/orbitals for electrons in closed and valence shells. Sturmian wave functions complement the basis functions and are used to describe virtual orbitals. The closed shells $1s^2$ and $2s^2$ of both Na atoms form the core of the homonuclear molecule. The superscript denotes the number of electrons in shell nl, where n is the principal quantum number and l is the orbital angular momentum. In our calculations excitations from these closed shells to valence and virtual orbitals are not included, i.e., all atomic determinants in the molecular basis contain the same number of electrons in these $1s$ and $2s$ orbitals. Single- and double-electron excitations from the closed $2p^6$ shells of Na atoms are allowed and introduce core-valence correlations in the CI. For relativistic calculations $2p^6$ is short for $2p_{1/2}^2 2p_{3/2}^4 \cdots$. The $3s$, $3p$, and $3d$ valence orbitals of Na are allowed to contain at most three electrons. In addition, we allow at most two electrons in $4s$, $4p$, $5s$, $5p$, $4d$, $5d$, $6s$, and $6p$ virtual orbitals. Both covalent and ionic configurations are constructed.

Figure 4 shows the absolute value of the transition dipole moments between the $X\ ^1\Sigma_g^+(0_g^+)$ ground state of Na_2 and two excited 0_u^+ states. Their values are listed in Tables IIa and IIb. At short-range internuclear separation, $R < 20a_0$, the excited states can be assigned by the nonrelativistic symmetries $A\ ^1\Sigma_{0_u^+}$ and $b\ ^3\Pi_{0_u^+}$. At long range the transition dipole moments become independent of R and their absolute values approach the Na $3s \rightarrow 3p(^2P_j)$ transition dipole moment when the corresponding excited potential dissociates to the $Na(3s)+Na(3p\ ^2P_j)$ limit. The sudden change in dipole moment in Fig. 4 near $7a_0$ is related to the avoided crossing

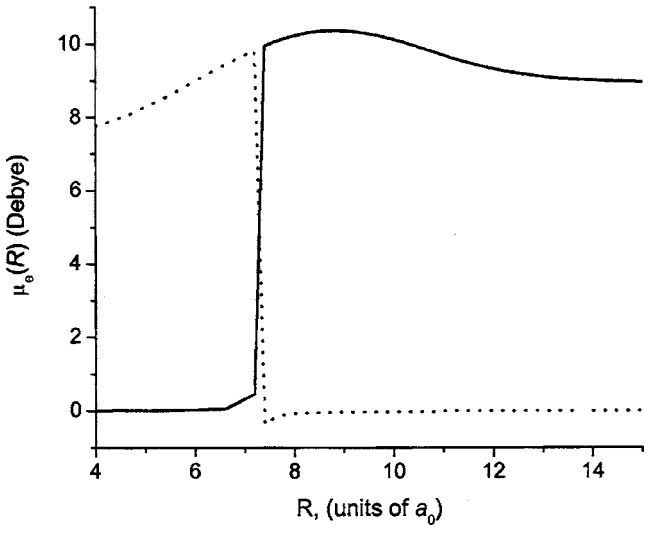

FIG. 4. Transition dipole moments between the ground $X\ ^1\Sigma_{0^+}$ and the $1(0_u^+)$ (solid line), $2(0_u^+)$ (dotted line) relativistic states of the Sodium dimer as function of internuclear separation obtained from relativistic *ab initio* calculations.

between the two excited $\Omega = 0_u^+$ potentials. This crossing is avoided due to the spin-orbit interaction, which couples the 0_u^+ components of the nonrelativistic $b\ ^3\Pi_u$ and $A\ ^1\Sigma_u^+$ potentials.

For a comparison with the experimental determination of the transition dipole moment matrix element for the X to A transition we have performed a nuclear-dynamics calculation. In order to evaluate this dipole moment matrix element we assume that the vibration of the Na dimer near the avoided crossing between the two excited 0_u^+ potentials is diabatic. That is, the vibrational energies are given by the eigenenergies of the nonrelativistic $A\ ^1\Sigma_u^+$ potential and that the transition dipole moment is determined from Fig. 4 by connecting the curve with nonzero dipole moment for $R < 7a_0$ and the curve with nonzero dipole moment for $R > 7a_0$. We perform the nuclear-dynamics calculations using a discrete variable representation (DVR) for the Schrödinger equation. The transition dipole moment matrix element is then given by the overlap between the wave functions and the R-dependent transition dipole moment.

Figure 5 shows the values of the transition dipole moment matrix elements as a function of the vibrational level of the $J'=21$ rotational state of the $X\ ^1\Sigma_g^+$ potential for the rovibrational level $v'=25$, $J'=20e$ of the $A\ ^1\Sigma_u^+$ potential. A clear maximum for the dipole moment is observed for vibrational level near $v''=38$.

3. Lifetime calculations

Due to the importance of the excited state lifetime values in our simulations, lifetimes for individual rovibrational levels of the $Na_2\ 2\ ^1\Pi_g$ as well as the $A\ ^1\Sigma_u^+$ state were calculated according to the general procedure outlined recently.[59] Because of the cubic frequency dependence of the transition probability there are two channels that completely dominate the spontaneous decay of the $2\ ^1\Pi_g$ state, namely, transitions to the $B\ ^1\Pi_u$ and $A\ ^1\Sigma_u^+$ states, which thus determine the radiative lifetime. For the numerical calculations of the decay

TABLE II. Tabulated absolute values of the transition dipole moments between the ground $X\,^1\Sigma_{0^+_g}$ and the $1(0^+_u)$ (a), $2(0^+_u)$ (b) relativistic states of Sodium dimer as function of the internuclear separation R using relativistic *ab initio* calculations.

R (a.u.)	$\mu_e(R)$ (D)	R (a.u.)	$\mu_e(R)$ (D)	R (a.u.)	$\mu_e(R)$ (D)
			(a)		
4.0	0.009 549	8.0	10.228 623	11.6	9.457 014
4.2	0.010 114	8.2	10.289 232	11.8	9.388 051
4.4	0.010 816	8.4	10.333 011	12.0	9.328 616
4.6	0.011 679	8.6	10.359 565	12.2	9.270 971
4.8	0.012 733	8.8	10.368 901	12.4	9.216 826
5.0	0.014 020	9.0	10.361 463	12.6	9.174 563
5.2	0.015 603	9.2	10.338 123	12.8	9.135 446
5.4	0.017 570	9.4	10.300 151	13.0	9.101 940
5.6	0.020 052	9.6	10.249 162	13.2	9.073 591
5.8	0.023 256	9.8	10.187 038	13.4	9.049 889
6.0	0.027 512	10.0	10.115 838	13.6	9.028 295
6.2	0.033 399	10.2	10.037 708	13.8	9.012 300
6.4	0.042 011	10.4	9.954 793	14.0	9.001 191
6.6	0.055 716	10.6	9.869 155	14.2	8.990 641
7.2	0.458 189	10.8	9.782 711	14.4	8.982 114
7.4	9.947 846	11.0	9.697 183	14.6	8.975 192
7.6	10.059 866	11.2	9.609 923	14.8	8.969 509
7.8	10.151 910	11.4	9.531 227	15.0	8.964 757
			(b)		
4.0	7.759 406	8.0	−0.068 442	11.6	2.4010^{-8}
4.2	7.844 888	8.2	−0.055 350	11.8	-5.7810^{-8}
4.4	7.938 605	8.4	−0.047 093	12.0	-3.2810^{-9}
4.6	8.042 081	8.6	−0.041 464	12.2	-1.6910^{-9}
4.8	8.155 195	8.8	−0.037 416	12.4	5.6310^{-10}
5.0	8.277 531	9.0	−0.034 425	12.6	1.6010^{-9}
5.2	8.408 208	9.2	−0.032 160	12.8	8.4510^{-10}
5.4	8.546 014	9.4	−0.030 431	13.0	3.7510^{-10}
5.6	8.689 517	9.6	−0.029 113	13.2	-9.3810^{-11}
5.8	8.837 140	9.8	−0.028 125	13.4	5.6310^{-10}
6.0	8.987 207	10	−0.027 412	13.6	1.7810^{-9}
6.2	9.137 979	10.2	−0.026 938	13.8	1.7810^{-9}
6.4	9.287 659	10.4	−0.026 683	14.0	7.5110^{-10}
6.6	9.434 406	10.6	−0.026 630	14.2	1.2210^{-9}
7.2	9.828 506	10.8	−0.026 772	14.4	1.5010^{-9}
7.4	−0.403 347	11.0	$1.271\,0^{-7}$	14.6	1.7810^{-9}
7.6	−0.146 6316	11.2	$1.171\,0^{-7}$	14.8	1.6010^{-9}
7.8	−0.092 0461	11.4	$1.531\,0^{-7}$	15.0	2.1610^{-9}

rates we used the computer program LEVEL 7.7 by Le Roy.[60] Potential-energy RKR curves for the relevant states, required in the program input, were available.[61–65] We used *ab initio* transition dipole moment functions between electronic states of Na_2. The program output gave the Einstein A coefficients for individual rotational emission lines from the $2\,^1\Pi_g$ ($v=25$, $J=20f$) level to the two lower states of interest. The calculated radiative lifetime for the $2\,^1\Pi_g$ ($v=25$, $J=20f$) level of Na_2 is (18.3±0.3) ns, where the reported error emanates from the estimated uncertainties in the transition energies and the transition dipole moments.

For the Na_2 $A\,^1\Sigma_u^+$ state many lifetimes have been experimentally determined by Baumgartner *et al.*[66] but none was available for the rovibrational levels used in this work. Therefore calculated lifetimes were also used for the A state in the simulations. For example, the calculated radiative lifetime for the $A\,^1\Sigma_u^+$ ($v'=25, J'=20e$) level of Na_2 is (12.5±0.3) ns. For control purposes calculations were performed for several levels in the present range of rovibrational quantum numbers, for which measured lifetimes are available. The average deviation between the calculated and observed lifetimes was ±1.4%.

V. RESULTS AND DISCUSSION

A. The three-level cascade excitation scheme

Figure 6(a) shows a probe laser scan for the excitation sequence $2\,^1\Pi_g$ ($v=3$, $J=14e$)←$A\,^1\Sigma_u^+$ ($v'=6$, $J'=13e$)←$X\,^1\Sigma_g^+$($v''=0$, $J''=14e$) followed by fluorescence decay to the $A\,^1\Sigma_u^+(v'=2, J'=13e)$ level [Fig. 1(a)]. In this case the k_1/k_2 ratio is 0.989. The Franck-Condon factors for the $A\,^1\Sigma_u^+$ ($v'=6$, $J'=13e$)-$X\,^1\Sigma_g^+$ ($v''=0$, $J''=14e$) and $A\,^1\Sigma_u^+$ ($v'=6$, $J'=13e$)-$2\,^1\Pi_g$ ($v=3$, $J=14e$) transitions are 0.101 and 0.035, respectively. The laser power values mea-

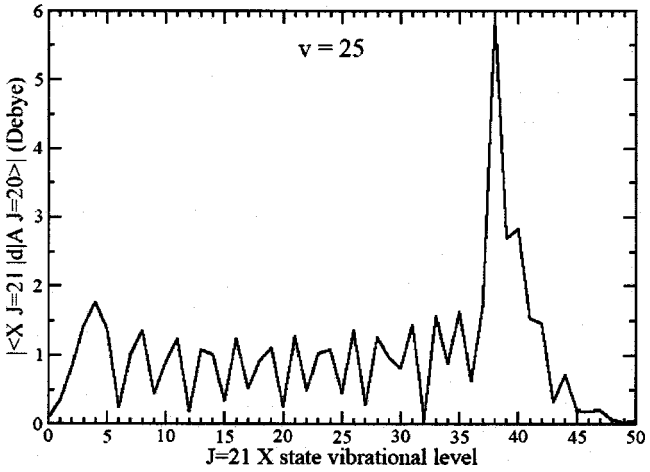

FIG. 5. Calculated transition dipole moment matrix elements for the rovibronic level $v'=25$, $J'=20e$ of the Sodium dimer $A\,^1\Sigma_u^+$ state potential as a function of the vibrational level of the $J''=21$ rotational state of the $X\,^1\Sigma_g^+$ potential.

sured in front of the heatpipe window were 270 and 7 mW for the coupling and probe laser fields, respectively. The spot sizes [defined as the diameter at which the intensity (proportional to the electric field squared) is reduced from its maximum value by a factor of $1/e^2$], for lasers L_1 and L_2, were 0.680 and 0.290 mm, respectively, leading to an effective value of ~480 MHz for the coupling field Rabi frequency in the center of the heatpipe. The 9% loss at the heatpipe window was included in this calculation. The simulated spectrum using the density matrix formalism is given in the same figure by a dotted line.

Figure 6(b) shows a probe laser scan of a single rovibronic fluorescence transition corresponding to the excitation sequence $2\,^1\Pi_g\,(v=4,\ J=14e) \leftarrow A\,^1\Sigma_u^+\,(v'=8,\ J'=13e) \leftarrow X\,^1\Sigma_g^+\,(v''=0,\ J''=14e)$ followed by fluorescence decay to $A\,^1\Sigma_u^+\,(v'=3,\ J'=13)$ level [Fig. 1(b)]. In this case the k_1/k_2 ratio is 1.011. The Franck-Condon factors for the $A\,^1\Sigma_u^+\,(v'=8,\ J'=13e)$-$X\,^1\Sigma_g^+\,(v''=0,\ J''=14e)$ and $2\,^1\Pi_g\,(v=4,\ J=14e)$-$A\,^1\Sigma_u^+\,(v'=8,\ J'=13e)$ transitions are 0.115 and 0.0090, respectively. The laser power values in front of the heatpipe were 160 and 1 mW for the L_1 and L_2 lasers, respectively, and the beam diameters (at $1/e^2$ points of the maximum intensity) are the same as above, leading to a coupling field Rabi frequency of ~390 MHz in the interaction region. The dotted line in the figure represents the corresponding simulated spectrum.

It is interesting to note that when the coupling field is tuned to resonance with the lower electronic transition $|1\rangle$ to $|2\rangle$ in the cascade case, the resolution of the AT splitting observed by using the fluorescence spectrum of level $|3\rangle$ is better resolved for $|k_1/k_2|>1$. When the coupling field is tuned to the upper transition $|2\rangle$ to $|3\rangle$, and a weak laser L_1 is scanned through the $|1\rangle$ to $|2\rangle$ resonance transition, the reverse is the case, as we have reported recently.[16,19] When $|k_1/k_2|<1$ the AT splitting in the fluorescence spectrum of a single rovibronic transition from level $|3\rangle$ is resolved and shows no AT splitting when $|k_1/k_2|>1$ for the moderate coupling laser Rabi frequencies used in our experiments. However, in both cases it appears that the AT splitting is resolved in the fluorescence spectrum from level $|3\rangle$ when the absolute value of the coupling field/probe laser wave number

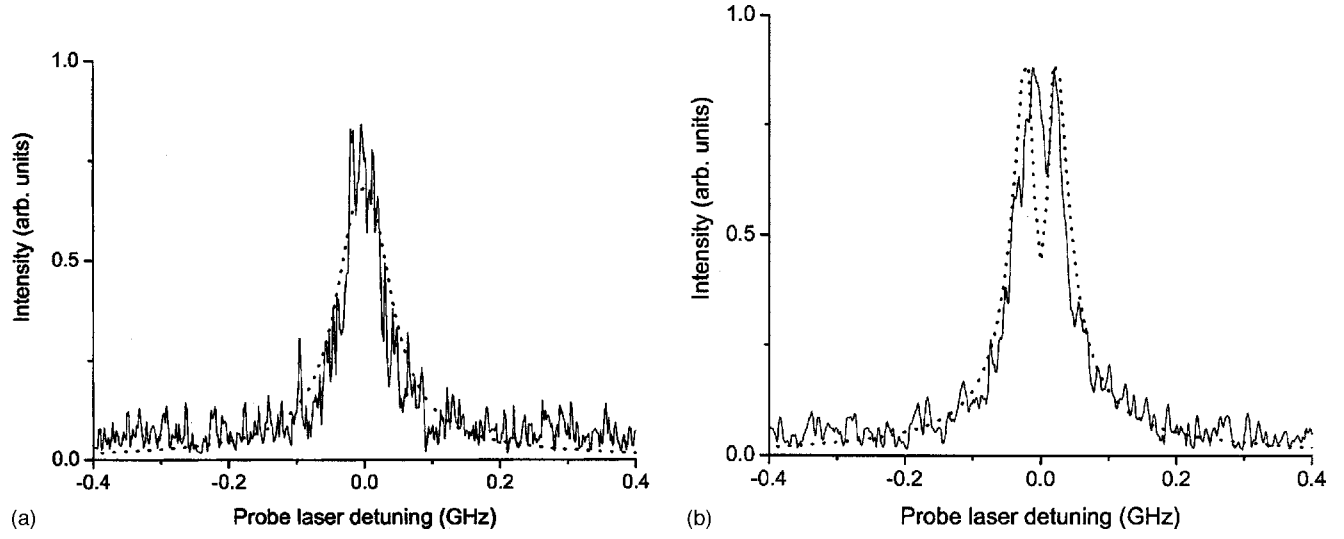

FIG. 6. Observed and simulated spectra with the energy level diagrams in Fig. 1. (a) The solid line is the recorded spectrum when using the excitation scheme shown in Fig. 1(a), where the wave number ratio $k_1/k_2=0.989$. The $2\,^1\Pi_g\,(v=3,\ J=14e) \rightarrow A\,^1\Sigma_u^+\,(v'=2,\ J'=13e)$ fluorescence was monitored while the probe laser L_2 was modulated and scanned. The probe laser and coupling field laser powers were 7 and 270 mW, respectively. The theoretical simulation of the spectrum is represented by a dotted line. The values of the parameters used in the simulations are lifetime of the $A\,^1\Sigma_u^+\,(v'=6,\ J'=13)$ level, $\tau_1=12.3$ ns, and lifetime of the $2\,^1\Pi_g\,(v'=3,\ J'=14e)$ level, $\tau_2=20.2$ ns; branching ratios $W_{32}/W_3=0.017$ and $W_{21}/W_2=0.050$; Doppler width of 1.15 GHz; collisional dephasing rates $\gamma_{12}/2\pi=1.59$ MHz and $\gamma_{13}/2\pi=\gamma_{23}/2\pi=4.77$ MHz; transit relaxation rate $w_t/2\pi=0.51$ MHz; and Rabi frequencies $\Omega_{23}=66$ MHz and $\Omega_{12}=480$ MHz corresponding to the experimental power values of probe and coupling field lasers in the interaction region, respectively. (b) Detecting the $2\,^1\Pi_g\,(v=4,\ J=14e) \rightarrow A\,^1\Sigma_u^+\,(v'=3,\ J'=13e)$ fluorescence when exciting the scheme in Fig. 1(b), where the wave number ratio $k_1/k_2=1.011$. Laser L_2 was modulated and scanned and the powers were 1 and 160 mW for the probe and coupling field lasers, respectively. The theoretical simulation of the spectrum is represented by the dotted line. The following values of the parameters were used in the simulations: lifetime of $A\,^1\Sigma_u^+\,(v'=8,\ J'=13e)$ level, $\tau_1=12.4$ ns, and lifetime of $2\,^1\Pi_g\,(v=4,\ J=14e)$ level, $\tau_2=20.0$ ns; branching ratios $W_{32}/W_3=0.0045$ and $W_{21}/W_2=0.058$; Doppler width and relaxation rates are the same as in Fig 6(a); and Rabi frequencies $\Omega_{23}=13$ MHz and $\Omega_{12}=390$ MHz corresponding to the (effective) experimental laser power values.

ratio is larger than 1. Further details on the conditions that lead to a low threshold Rabi frequency for AT splitting in a Doppler-broadened medium in terms of the wavelength dependence of the laser fields and the role of laser beam geometry in the three-level cascade excitation scheme will be reported in a forthcoming publication.[19]

B. The four-level triple resonance excitation scheme

Figure 2(a) illustrates the energy level diagram of our four-level (triple resonance) extended Λ excitation scheme. In this case the pump (L_1) and the probe (L_2) lasers copropagate. Laser L_3 is the coupling field, which counterpropagates with L_1 and L_2. Level $|1\rangle X\ ^1\Sigma_g^+\ (v''=1,\ J''=19e)$ is the initial level of the pump laser L_1, and level $|2\rangle A\ ^1\Sigma_u^+\ (v'=25,\ J'=20e)$ is the final level of the pump laser L_1 and also the upper/lower level of the coupling field L_3/probe laser L_2, respectively. Level $|3\rangle 2\ ^1\Pi_g\ (v=25,\ J=20f)$ is the upper level of the probe laser L_2 and level $|4\rangle X\ ^1\Sigma_g^+\ (v''=38,\ J''=21e)$ is the lower level of the coupling field. We have chosen a high vibrational level of the ground state outside the range of thermally populated levels for this purpose. The Franck-Condon factors of the $A\ ^1\Sigma_u^+\ (v'=25,\ J'=20e)$-$X\ ^1\Sigma_g^+\ (v''=1,\ J''=19e)$, $2\ ^1\Pi_g\ (v=25,\ J=20f)$-$A\ ^1\Sigma_u^+\ (v'=25,\ J'=20e)$, and $A\ ^1\Sigma_u^+\ (v'=25,\ J'=20e)$-$X\ ^1\Sigma_g^+\ (v''=38,\ J''=21e)$ transitions are 0.0020, 0.076, and 0.32, respectively. The populations in the intermediate and upper states were monitored by detecting the $A\ ^1\Sigma_u^+\ (v'=25,\ J'=20e)\rightarrow X\ ^1\Sigma_g^+\ (v''=4,\ J''=21e)$ and $2\ ^1\Pi_g\ (v=25,\ J=20f)\rightarrow A\ ^1\Sigma_u^+\ (v'=20,\ J'=20e)$ fluorescences, respectively. The spot sizes were 560, 460, and 1020 μm (diameter) for the pump laser (L_1), probe laser (L_2), and coupling field (L_3) laser beams, respectively.

In the experiments based on this excitation scheme the power of the pump and probe lasers was kept constant while the power of the coupling laser was varied. The goal was to investigate how the AT splitting features in the fluorescence excitation spectra from level $|3\rangle$ depend on the coupling laser power. In order to minimize the influence of the pump L_1 and probe L_2 lasers on the AT effect their power was kept as low as possible, while still having a good signal-to-noise ratio in the recorded spectra. By varying the powers of lasers L_1 and L_2 we found that the combination of laser powers of ~40 and ~5 mW for L_1 and L_2, respectively, at the given laser beam spot sizes had a minimal effect on the observed AT splitting spectrum and the signal-to-noise ratio in the spectra was acceptable. Further, the power of the coupling laser L_3 was changed between 100 and 450 mW with the aid of neutral density filters while the power of the other two lasers was kept constant. As shown in Fig. 7, the experiments indicate that there is a linear dependence between the observed Autler-Townes splitting and the coupling field Rabi frequency, as is expected. In contrast to Ref. 16, we emphasize here the use of the *R*-centroid approximation for calculating the *R*-dependent electronic transition dipole moment from the transition dipole moment matrix element, which is determined from the value of the Rabi frequency, that best characterizes the observed AT splitting spectral pattern. We should also note here that while in Ref. 16 the coupling

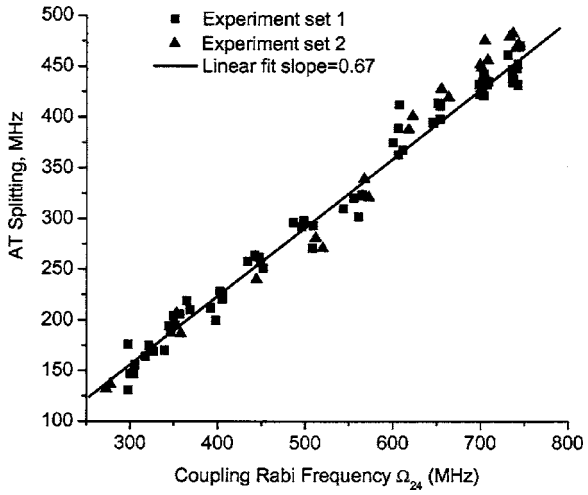

FIG. 7. The Autler-Townes splitting observed in the fluorescence spectrum from level $|3\rangle$ in the extended lambda scheme experiment vs the coupling field Rabi frequency Ω_{24} on the $A\ ^1\Sigma_u^+\ (v'=25,\ J'=20e)$-$X\ ^1\Sigma_g^+\ (v''=38,\ J''=21e)$ transition. Parameters used in the theoretical simulations: pump and probe laser Rabi frequencies $\Omega_{12}=28$ MHz and $\Omega_{23}=52$ MHz, respectively; collisional dephasing rates $\gamma_{12}/2\pi=\gamma_{24}/2\pi=\gamma_{14}/2\pi=\gamma_{13}/2\pi=\gamma_{23}/2\pi=\gamma_{34}/2\pi=4.77$ MHz. The transition dipole moment matrix element $\mu=(5.5\pm0.2)$ D obtained from the best agreement between the density matrix theory and experimental spectra along with the linear fit from this graph gives us the relationship between the AT splitting and the coupling electric field E_3 to be AT splitting$=0.67\mu E_3/\hbar$ for the $A\ ^1\Sigma_u^+\ (v'=25,\ J'=20e)$-$X\ ^1\Sigma_g^+\ (v''=38,\ J''=21e)$ transition. Note that the coefficient 0.67 will change for different rovibrational transitions and depends on the type of the transition (…, *P*,*Q*,*R*, …), wavelength of the lasers involved and the rotational quantum numbers of the states coupled by the coupling, probe, and pump lasers.

transition is between rovibrational levels of two excited electronic states, in this case the coupling laser couples a rovibrational level from the ground state to a rovibrational level from the first excited electronic state. Here our purpose was to develop a generally applicable method to measure accurately and reliably the transition dipole moment function between the ground and excited states. We demonstrate our method in detail by determining the transition dipole moment matrix element for the $A\ ^1\Sigma_u^+\ (v'=25,\ J'=20e)$-$X\ ^1\Sigma_g^+\ (v''=38,\ J''=21e)$ transition of Na_2.

First an OODR spectrum of the pump L_1 and probe L_2 lasers is recorded, as shown on Fig. 8(a). The OODR spectrum is simulated with the density matrix formalism to verify that the parameters used later in the model to simulate the AT splitting spectra are correct. These include the calculated lifetimes of the excited states, the Franck-Condon factors of the pump and probe transitions, the collisional dephasing rates, etc. This signal was recorded as a function of the probe laser L_2 detuning while the pump laser L_1 was kept on resonance. The laser power values of L_1 and L_2 were reduced to 40 and 5 mW, respectively, resulting in a linewidth full width at half maximum [(FWHM)] of ~160 MHz. Figure 8(b) shows a sample AT split OODR excitation line in the presence of the coupling field, observed when L_1 and L_3 were held fixed on resonance and L_2 was modulated and scanned. The spectrum corresponds to a coupling field power of 450 mW. In simulations using the density matrix formalism the pump and probe laser Rabi frequencies were determined by the experimental laser power values in the interaction region,

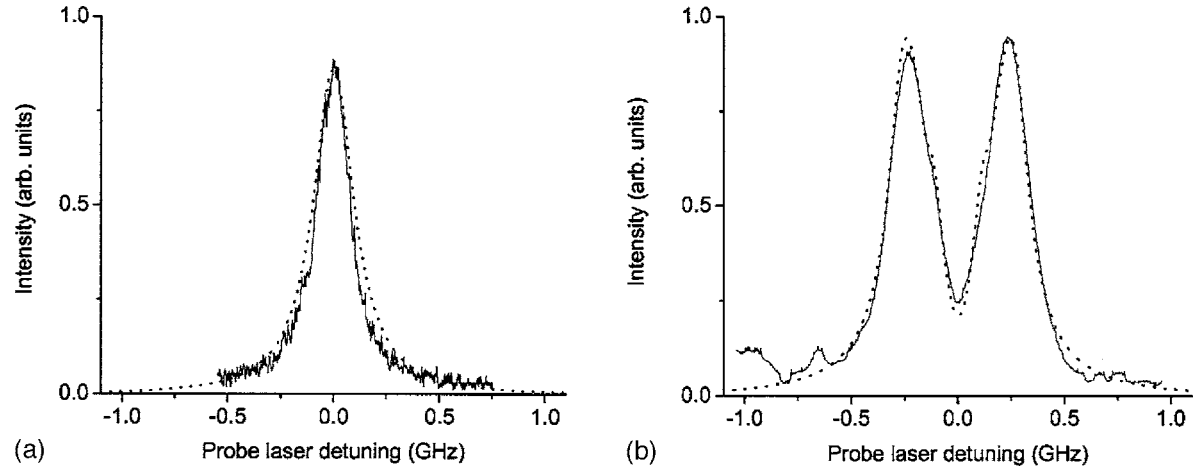

FIG. 8. Spectra observed using the extended lambda excitation scheme of Fig. 2(a) and monitoring the $2\ ^1\Pi_g\ (v=25,\ J=20f) \rightarrow A\ ^1\Sigma_u^+\ (v'=20,\ J'=20e)$ fluorescence as a function of the detuning of the probe laser. Theoretical simulations are performed as described in Sec. IV with the following common parameters: lifetime of the $A\ ^1\Sigma_u^+\ (v'=25,\ J'=20e)$ level, $\tau_2=12.5$ ns, and lifetime of the $2\ ^1\Pi_g\ (v=25,\ J=20f)$ level, $\tau_3=18.3$ ns; branching ratios $W_{32}/W_3=0.076$, $W_{21}/W_2=0.001$, and $W_{24}/W_2=0.16$; Doppler width of 1.15 GHz; collisional dephasing rates $\gamma_{12}/2\pi=\gamma_{24}/2\pi=\gamma_{14}/2\pi=\gamma_{13}/2\pi=\gamma_{23}/2\pi=\gamma_{34}/2\pi=4.77$ MHz; and transit relaxation rate $w_t/2\pi=0.38$ MHz. (a) The OODR excitation line shape without the coupling laser when the pump L_1 was held fixed at resonance frequency and the probe laser L_2 was modulated and scanned. The powers of L_1 and L_2 were 40 and 5 mW, respectively, leading to a linewidth (FWHM) of ~160 MHz. In the simulation the values of the corresponding (effective) Rabi frequencies were $\Omega_{12}=28$ MHz and $\Omega_{23}=52$ MHz, respectively. (b) Fluorescence spectrum recorded when pump and coupling field lasers L_1 and L_3 were held fixed on resonance and the probe laser L_2 was modulated and scanned. In this case the coupling laser power (before heatpipe) was 450 mW, while the pump and probe laser powers were held at 40 and 5 mW, respectively. The corresponding (effective) values of the Rabi frequencies were $\Omega_{12}=28$ MHz and $\Omega_{23}=52$ MHz in the simulation. The comparison of the simulated AT splitting pattern with the experimental spectrum yields the best value of the coupling field Rabi frequency $\Omega_{24}=755$ (±10) MHz.

whereas the Rabi frequency of the coupling field Ω_{24} is obtained from the best fit to the recorded experimental spectrum. This Ω_{24} value along with the strength of the coupling laser electric field E_3 is used to calculate the transition dipole moment matrix element between the rovibrational levels coupled by E_3. For the coupling laser electric field amplitude we use the value of the E field at the center of the Gaussian distribution calculated from the measured total coupling laser power using the expression

$$E=\sqrt{\frac{2}{c\varepsilon_0}}\sqrt{\frac{8P}{\pi w^2}},$$

where P is the measured laser power, and w is the spot size diameter at which the intensity (proportional to the electric field squared) is reduced from its maximum value by a factor of $1/e^2$. This is an approximation based on the assumption that in the region, where the probe and pump fields have significant contributions to the detected signal, the coupling laser electric field has a uniform distribution with a value given by the above expression. The error due to this approximation is not significant, because in the experiments the diameters of the probe and pump beams were chosen to be small enough compared to the diameter of the coupling laser beam. The main contribution to the error in the electric field determination arises from the experimental error in the measurement of the spot size w and the total laser power P. For a coupling laser spot size of 1020 μm and power level of 100 to 500 mW the relative error in electric field is 3.5%.

To determine the transition dipole moment matrix element we used $\Omega=\mu E/\hbar$ for the Rabi frequency. The Rabi frequencies were determined from the density matrix equations-of-motion simulations for spectra observed with coupling laser power ranging from 100 to 450 mW. The resulting transition dipole moment matrix element $\mu=5.5\pm0.2$ D is an average of the transition dipole moment matrix elements determined from these spectra for the $Na_2\ A\ ^1\Sigma_u^+\ (v'=25,\ J'=20e)$-$X\ ^1\Sigma_g^+\ (v''=38,\ J''=21e)$ coupling laser transition. The error in the value of μ arises mainly from the error in the measurement of the spot sizes (±10 μm), the laser power fluctuation (1%–2%), and the inherent noise in the recorded spectra. The experimental AT splitting values are shown in Fig. 7 as a function of the coupling laser Rabi frequency, confirming the linear dependence $0.67\mu E_3/\hbar$ of the Autler-Townes splitting on the coupling laser electric field amplitude E_3. Figure 3 illustrates the electronic transition dipole moment $\mu_e(R)$ and the vibrational wave functions in the R-centroid region of the coupling field transition. The calculated R-centroid value for the coupling field transition is 4.81 Å. By using the R-centroid approximation the experimentally measured transition dipole moment matrix element is 5.5±0.2 D and yields a value of 9.72 D at $R_c=4.81$ Å for the electronic transition moment $\mu_e(R_c)$. The corresponding *ab initio* result at this R-centroid value is 10.55 D. The agreement is about the same between the measured and *ab initio* transition dipole moment *matrix elements* of 5.5 and 5.9 D, respectively, indicating that the measured transition dipole moment matrix element information can be readily converted to the R-dependent electronic transition dipole moment function $\mu_e(R)$. To provide a more complete picture of the $\mu_e(R)$ function R dependence in this case experiments are in progress for other v', v'' coupling laser transitions. Figure 9 shows a theoretical reconstruction of the electronic transition dipole moment function based on calculated transition dipole moment matrix elements divided by the vibrational overlap factor. The pattern is very similar to that indicated by Noda and Zare[43] for the same molecular

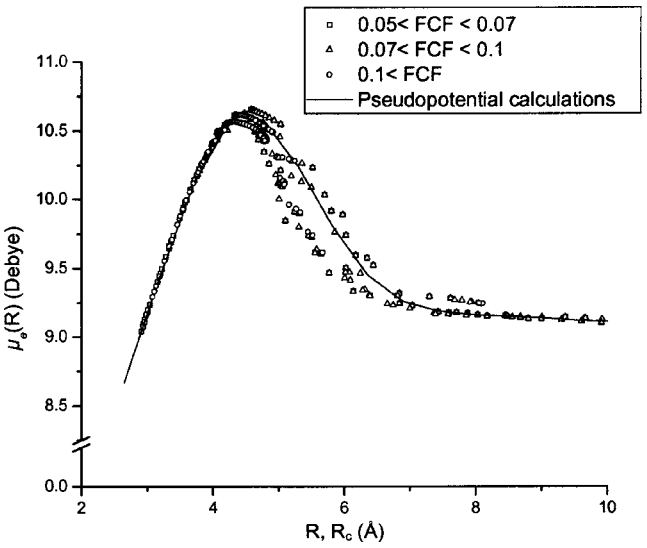

FIG. 9. Reconstruction of the electronic transition dipole moment based on the *R*-centroid approximation. Calculated transition dipole moment matrix elements, based on the pseudopotential calculated $\mu_e(R)$ function, divided by the vibrational overlap factor, are shown as a function of the corresponding calculated *R*-centroid values. For comparison, the *ab initio* electronic transition moment is shown as a function of internuclear distance *R*.

transition. In order to resolve problems with multiple points of stationary phase we plan to apply the generalized *R*-centroid method[43] by segmenting the numerical integration.

VI. CONCLUSIONS

We have presented a novel and generally applicable method that combines the advantages of the Autler-Townes quantum interference effect with the *R*-centroid approximation to measure the absolute value of the transition dipole moment matrix element for molecular transitions between the ground and excited states. We have demonstrated this method experimentally by using $Na_2\, A\, ^1\Sigma_u^+\, (v'=25,\, J'=20e)$-$X\, ^1\Sigma_g^+\, (v''=38,\, J''=21e)$ molecular transition as an example using a Doppler broadened sample. Two excitation schemes, the three-level cascade and the four-level extended Λ excitation scheme, were compared to determine which configuration is most favorable for this purpose. Our results indicate that the extended Λ scheme is preferable for the moderate coupling field Rabi frequencies available with continuous wave laser sources. Within the extended Λ excitation scheme, the lower level of the coupling field is outside the thermal population range. Such vibrational levels with large wave function amplitudes at the outer turning point of molecular vibration lead to large transition dipole moment matrix elements and as a result to a larger Rabi frequency for the coupling laser transition. In addition, compared to the three-level excitation scheme with the coupling laser tuned to the lower transition, the weak pump laser also defines a much narrower velocity group within the Doppler profile, leading to better resolved AT splitting of the intermediate level.

The three-level cascade system suffers from a loss in resolution in the AT splitting spectrum, because the strong coupling field excites a broader velocity group for the probe laser scan. In addition, since the initial level of the coupling laser is within the thermal distribution of the ground state, the transition dipole moment matrix elements of the coupling laser transition are less favorable due to smaller wavefunction amplitudes at the vibrational turning points in the excited state vibrational levels accessible from the thermal population internuclear range.

By using the four-level extended lambda excitation scheme, the coupling laser can be "tuned" to different rovibronic transitions in order to determine the internuclear distance dependence of the transition dipole moment function in the region of the *R*-centroid of each coupling laser transition. Thus the internuclear distance dependence of the electronic transition moment function $\mu_e(R)$ can be determined at several very different values of the *R*-centroid. The measured transition dipole moment matrix element for the $Na_2\, A\, ^1\Sigma_u^+\, (v'=25,\, J'=20e)$-$X\, ^1\Sigma_g^+\, (v''=38,\, J''=21e)$ transition is 5.5 ± 0.2 D compared to our *ab initio* value of 5.9 D. By using the *R*-centroid approximation for this transition the corresponding experimental electronic transition dipole moment is 9.72 D at $R_c=4.81$ Å in good agreement with our *ab initio* value of 10.55 D.

In the future, we wish to include the spin-orbit mixing between the $2(0_u^+)$ and $3(0_u^+)$ states via nonadiabatic coupling in our calculation of the transition dipole moment in an effort to provide a more stringent comparison with the experiment. In addition, similar comparisons with the experiment and theory in cases where the spin-orbit interaction is much weaker or much stronger such as Li_2 and K_2, respectively, will give additional information on the importance of the relativistic effects.

ACKNOWLEDGMENTS

This work was supported by National Science Foundation Awards PHY 0245311 and PHY 0216187. One of the authors (A.H.) gratefully acknowledges support from Stockholm University during her visit to Temple University. Two of the authors (A.H. and L.L.) were also supported in part by the Lagerqvist Research Fund of Temple University during their visits. One of the authors (L.L.) also acknowledges support from NSFC (20473042) and NKBRSF of China. The authors thank Professor Frank Spano for providing the computer program used for the simulations presented in this work and are grateful for valuable discussions with Professor R. W. Field.

[1] S. E. Harris, J. E. Field, and A. Imamoglu, Phys. Rev. Lett. **64**, 1107 (1990); K.-J. Boller, A. Imamoglu, and S. E. Harris, *ibid.* **66**, 2593 (1991).
[2] S. H. Autler and and C. H. Townes, Phys. Rev. **100**, 703 (1955).
[3] J. Gea-Banacloche, Y. Li, S. Jin, and M. Xiao, Phys. Rev. A **51**, 576 (1995).
[4] D. J. Fulton, S. Shepherd, R. R. Moseley, B. D. Sinclair, and M. H. Dunn, Phys. Rev. A **52**, 2302 (1995).
[5] F. S. Cataliotti, C. Fort, T. W. Hansch, M. Inguscio, and M. Prevedelli, Phys. Rev. A **56**, 2221 (1997).
[6] D. McGloin, D. J. Fulton, and M. H. Dunn, Opt. Commun. **190**, 221 (2001).
[7] J. H. Xu, G. C. La Rocca, F. Bassani, D. Wang, and J. Y. Gao, Opt. Commun. **216**, 157 (2003).
[8] D. McGloin, J. Phys. B **36**, 2861 (2003).
[9] M. Yan, E. G. Rickey, and Y. Zhu, Phys. Rev. A **64**, 43807 (2001).

[10] A. Joshi and M. Xiao, Phys. Lett. A **317**, 370 (2003).
[11] M. A. Quesada, A. M. F. Lau, D. H. Parker, and D. W. Chandler, Phys. Rev. A **36**, 4107 (1987).
[12] B. Girard, G. O. Sitz, R. N. Zare, N. Billy, and J. Vique, J. Chem. Phys. **97**, 26 (1992).
[13] S. Xu, G. Sha, B. Jiang, W. Sun, X. Chen, and C. Zhang, J. Chem. Phys. **100**, 6122 (1994).
[14] N. N. Rubtsova, Opt. Spectrosc. **91**, 53 (2001).
[15] J. Qi, G. Lazarov, X. Wang, L. Li, L. M. Narducci, A. M. Lyyra, and F. C. Spano, Phys. Rev. Lett. **83**, 288 (1999).
[16] J. Qi, F. C. Spano, T. Kirova, A. Lazoudis, J. Magnes, L. Li, L. M. Narducci, R. W. Field, and A. M. Lyyra, Phys. Rev. Lett. **88**, 173003 (2002).
[17] F. Benabid, P. S. Light, F. Couny, and P. S. Russell, Opt. Express **13**, 5694 (2005).
[18] S. Ghosh, J. E. Sharping, D. G. Ouzounov, and A. L. Gaeta, Phys. Rev. Lett. **94**, 093902 (2005).
[19] E. Ahmed *et al.* (unpublished); see also A. Lazoudis, E. Ahmed, L. Li, T. Kirova, P. Qi, A. Hansson, J. Magnes, F. C. Spano, and A. M. Lyyra, e-print quant-ph/0508110.
[20] P. Yi, M. Song, Y. Liu, R. W. Field, L. Li, and A. M. Lyyra, Opt. Commun. **233**, 131 (2004).
[21] L. Li, P. Qi, A. Lazoudis, E. Ahmed, and A. M. Lyyra, Chem. Phys. Lett. **403**, 262 (2005).
[22] R. Garcia-Fernandez, A. Ekers, J. Klavins, L. P. Yatsenko, N. N. Bezuglov, B. W. Shore, and K. Bergmann, Phys. Rev. A **71**, 023401 (2005).
[23] B. Laburthe Tolra, C. Drag, and P. Pillet, Phys. Rev. A **64**, 061401(R) (2001).
[24] U. Schloder, T. Deuschle, C. Silber, and C. Zimmermann, Phys. Rev. A **68**, 051403(R) (2003).
[25] K. Winkler, G. Thalhammer, M. Theis, H. Ritch, R. Grimm, and J. Hecker Denschlag, Phys. Rev. Lett. **95**, 063202 (2005).
[26] F. C. Spano, J. Chem. Phys. **114**, 276 (2001).
[27] A. M. Lyyra, H. Wang, T.-J. Wang, L. Li, and W. C. Stwalley, Phys. Rev. Lett. **66**, 2724 (1991); A. M. Lyyra, P. D. Kleiber, and W. C. Stwalley, in *Molecular Dynamics and Spectroscopy by Stimulated Emission Pumping*, Advanced Series in Physical Chemistry Vol. 4, edited by H.-L. Dai and R. W. Field (World Scientific, Singapore, 1995), pp. 459–490.
[28] M. M. Hessel, E. W. Smith, and D. E. Drullinger, Phys. Rev. Lett. **33**, 1251 (1974).
[29] J. Tellinghuisen, J. Chem. Phys. **58**, 2821 (1973); **76**, 4736 (1982).
[30] For recent examples, see M. Lamrini, R. Bacis, D. Cerny, S. Churassy, P. Crozet, and A. J. Ross, J. Chem. Phys. **100**, 8780 (1994); P. Burns, L. Sibbach-Morgus, A. D. Wilkins, F. Halpern, L. Clarke, R. D. Miles, L. Li, A. P. Hickman, and J. Huennekens, *ibid.* **119**, 4743 (2003).
[31] J. Brzozowski, N. Elander, P. Erman, and M. Lyyra, Astrophys. J. **193**, 741 (1974).
[32] M. Tamanis, M. Auzinsh, I. Klincare, O. Nikolayeva, R. Ferber, A. Zaitsevskii, E. A. Pazyuk, and A. V. Stolyarov, J. Chem. Phys. **109**, 6725 (1998).
[33] P. Erman, Astrophys. J. **213**, L89 (1977).
[34] J. B. Koffend, R. Bacis, and R. W. Field, J. Chem. Phys. **70**, 2366 (1979).
[35] P. A. Frazer, Can. J. Phys. **32**, 516 (1954).
[36] H. Klemsdal, Phys. Norv. **5**, 123 (1971).
[37] R. W. Nichols, Chem. Phys. Lett. **17**, 252 (1972).
[38] R. W. Nichols, Chem. Phys. Lett. **20**, 261 (1973).
[39] R. W. Nichols, J. Quant. Spectrosc. Radiat. Transf. **14**, 233 (1973).
[40] S. M. Yazykova and E. V. Buturskaya, J. Phys. B **13**, 3361 (1980).
[41] J. Tellinghuisen, J. Mol. Spectrosc. **103**, 455 (1984).
[42] J. Tellinghuisen, in *The Franck-Condon Principle in Bound-Free Transitions*, Advances in Chemical Physics Vol. 60, edited by K. P. Lawley (John Wiley & Sons, New York, 1985), pp. 299-369.
[43] C. Noda and R. N. Zare, J. Mol. Spectrosc. **95**, 254 (1982).
[44] J. Tellinghuisen, J. Chem. Phys. **106**, 1305 (1997).
[45] D. R. Skinner and R. E. Whitcher, J. Phys. E **5**, 237 (1972).
[46] J. M. Brown, J. T. Hougen, K. P. Huber, J. W. C. Johns, I. Kopp, H. Lefebvre-Brion, A. J. Merer, D. A. Ramsey, J. Rostas, and R. N. Zare, J. Mol. Spectrosc. **55**, 500 (1975).
[47] H. Lefebvre-Brion and R. W. Field, *The Spectra and Dynamics of Diatomic Molecules* (Elsevier, New York, 2004).
[48] L. M. Narducci, M. O. Scully, G.-L. Oppo, P. Ru, and J. R. Tredicce, Phys. Rev. A **42**, 1630 (1990).
[49] A. S. Manka, H. M. Doss, L. M. Narducci, P. Ru, and G.-L. Oppo, Phys. Rev. A **43**, 3748 (1991).
[50] R. W. Boyd, *Nonlinear Optics* (Academic Press, Boston, 1992).
[51] S. Stenholm, *Foundations of Laser Spectroscopy* (Wiley Interscience, New York, 1984).
[52] J. Sagle, R. K. Namiotka, and J. Huennekens, J. Phys. B **29**, 2629 (1996).
[53] S. Magnier, Ph. Millié, O. Dulieu, and F. Masnou-Seeuws, J. Chem. Phys. **98**, 7113 (1993).
[54] S. Kotochigova, E. Tiesinga, and I. Tupitsyn, *New Trends in Quantum Systems in Chemistry and Physics* (Kluwer Academic, The Netherlands, 2001), Vol. 1, pp. 219–242.
[55] T.-J. Whang, W. C. Stwalley, L. Li, and A. M. Lyyra, J. Chem. Phys. **97**, 7211 (1992).
[56] E. Tiemann, H. Knockel, and H. Richling, Z. Phys. D: At., Mol. Clusters **37**, 323 (1996).
[57] C. Samuelis, E. Tiesinga, T. Laue, M. Elbs, H. Knockel, and E. Tiemann, Phys. Rev. A **63**, 012710 (2000).
[58] N. Okada, S. Kasahara, T. Ebi, M. Baba, and H. Kato, J. Chem. Phys. **105**, 3458 (1996).
[59] A. Hansson and J. G. Watson, J. Mol. Spectrosc. **233**, 169 (2005).
[60] R. J. Le Roy, University of Waterloo Chemical Physics Research Report No. CP661, 2005.
[61] C.-C. Tsai, Ph.D. thesis, University of Iowa, 1993.
[62] P. Kusch and M. M. Hessel, J. Chem. Phys. **68**, 2591 (1978).
[63] E. Tiemann, Z. Phys. D: At., Mol. Clusters **5**, 77 (1987).
[64] E. Tiemann, H. Knockel, and H. Richling, Z. Phys. D: At., Mol. Clusters **37**, 323 (1996).
[65] H. Richter, H. Knockel, and E. Tiemann, Chem. Phys. **157**, 217 (1991).
[66] G. Baumgartner, H. Kornmeier, and W. Preuss, Chem. Phys. Lett. **107**, 13 (1984).